Soft Matter

Shear-Induced Migration of Confined Flexible Fibers

Journal:	*Soft Matter*
Manuscript ID	SM-ART-08-2021-001256.R1
Article Type:	Paper
Date Submitted by the Author:	17-Oct-2021
Complete List of Authors:	Xue, Nan; Princeton University, Department of Mechanical and Aerospace Engineering Nunes, Janine; Princeton University, Department of Mechanical and Aerospace Engineering Stone, Howard; Princeton University, Department of Mechanical and Aerospace Engineering

Soft Matter

ARTICLE TYPE

Cite this: DOI: 00.0000/xxxxxxxxxx

Shear-Induced Migration of Confined Flexible Fibers†

Nan Xue,[a] Janine K. Nunes,[a] and Howard A. Stone*[a]

Received Date
Accepted Date

DOI: 00.0000/xxxxxxxxxx

We report an experimental study of the shear-induced migration of flexible fibers in suspensions confined between two parallel plates. Non-Brownian fiber suspensions are placed and imaged in a rheo-microscopy setup, where the top and the bottom plates counter-rotate and create a Couette flow. Initially, the fibers are near the bottom plate due to sedimentation. Under shear, the fibers move with the flow and migrate towards the center plane between the two walls. Statistical properties of the fibers, such as the mean values of the positions, orientations, and end-to-end lengths of the fibers, are used to characterize the behaviors of the fibers. A dimensionless parameter Λ_{eff}, which compares the hydrodynamic shear stress and the fiber stiffness, is used to analyze the effective flexibility of the fibers. The observations show that the fibers that are more likely to bend exhibit faster migration. As Λ_{eff} increases (softer fibers and stronger shear stresses), the fibers tend to align in the flow direction and the motions of the fibers transition from tumbling and rolling to bending. The bending fibers drift away from the walls to the center plane. Further increasing Λ_{eff} leads to more coiled fiber shapes, and the bending is more frequent and with larger magnitudes, which leads to more rapid migration towards the center. Different behaviors of the fibers are quantified with Λ_{eff}, and the structures and the dynamics of the fibers are correlated with the migration.

1 Introduction

The interactions between fibers and flows are ubiquitous and essential in many biological processes in nature[1]. For example, micro-organisms use their flagella for swimming[2,3]; diving beavers use their hair to entrain air and keep warm[4]; in humans, dense arrays of cilia pump fluids into lungs[5]. Fiber-flow interactions are also widely utilized in applications, such as stretching and breaking DNA molecules in a microfluidic channel[6], designing and controlling swimming robots via electrical forcing[7], and making soft materials by fiber entanglements[8].

The dynamics of fibers are rich but complex: fibers roll, tumble, bend, buckle, coil, entangle, and even break in flows[1,6,8–22]. For a non-Brownian fiber that moves freely in a viscous shear flow, the dynamics of the fibers are mainly governed by the competition between the hydrodynamic forcing and the fiber stiffness. As a scaling argument, by comparing the viscous forcing and fiber bending stiffness, we achieve a dimensionless parameter Λ_{eff}, which we denote as the effective flexibility of the fibers in this article, i.e.,

$$\Lambda_{\text{eff}} = \frac{64\eta\dot{\gamma}L^4}{\pi E D^4}, \tag{1}$$

where η is the viscosity of the liquid, $\dot{\gamma}$ is the shear rate of the flow, L is the length of the fiber, D is the diameter of the fiber, and E is the Young's modulus of the fiber. The expression of Λ_{eff} in Eq. (1) is similar to the expressions in Refs. 1, 8, 9, 13, and 14, though it is also usual to take the inverse of Λ_{eff} to demonstrate the effective stiffness of the fibers (the symbol is usually S_{eff}). Equation (1) indicates that the fibers are more likely to bend when the shear stress $\eta\dot{\gamma}$ is large, the aspect ratio of the fiber L/D is large, and the Young's modulus is small. We note that in this article, the descriptions *flexible fibers* and *bendable fibers* indicate that the fibers have a large aspect ratio, $L/D \gg 1$ and $\Lambda_{\text{eff}} \gg 1$.

The behavior of fibers in shear flows can be complex. To analyze the behavior of a single fiber, geometric parameters of the fibers, such as the end-to-end vector and radius of curvature, are usually used as the signatures of the fiber dynamics[1,10,16,19,21,22]. For example, the periodic dynamics of a fiber can be resolved by tracking (the orientation or length of) the end-to-end vector as a function of time[16,19,21]: a rolling fiber maintains the same orientation as well as the same end-to-end length; for a tumbling fiber, the orientation of the fiber changes as a function of time, while the end-to-end length is constant; for flexible fibers that bend in shear flows, both the orientations and end-to-end lengths change in time. Further, an increase in shear rate leads to effectively more deformed fibers and a decrease in the radius of curvature of the fibers[10,22].

The macroscopic rheology of fiber suspensions is another signature of the behavior of fibers in shear flows and is of interest to many industrial applications[23,24]. The rheology of the fiber suspensions is connected to the microscopic behaviors of

[a] Department of Mechanical and Aerospace Engineering, Princeton University, Princeton, NJ 08544, USA; E-mail: hastone@princeton.edu

† Electronic Supplementary Information (ESI) available. See DOI:

the fibers[25,26]. Thus, controlling the microscopic behavior of the fibers has the potential to design fiber suspensions with desired rheological properties[8].

In shear flows, the particles in non-colloidal and colloidal suspensions tend to migrate due to non-linear effects, such as viscoelasticity[27–29], inertia[30,31], particle-particle interactions[32], and wall effects[33–45]. For example, spherical particles migrate and assemble patterns in viscoelastic liquid[27–29], and polymers migrate laterally towards the center in a microfluidic channel[39–41,45]. Note that chaotic flow can also lead to irreversibility and particle migration[46]. Moreover, flexible structures make a Stokes flow irreversible. For example, a deformable wall[47] or deformable particles[34,36,37] can lead to the drifting of the particles away from the walls. Also, it has been suggested by numerical simulations that a non-Brownian flexible fiber in a shear flow would migrate away from the wall[15].

In applications, a typical scenario is that a suspension of non-Brownian flexible fibers flows in a channel or pipe. Sometimes, the length of the fibers is of the same order of magnitude as the cross-sectional size (height, width, or radius) of the channel, though the diameter of the fibers is much smaller[8,23]. It is our understanding that in a geometry where the fiber suspension is confined between the walls, the shear-induced migration of non-Brownian fibers is not yet fully understood: the effects of the flexibility of the fibers and the corresponding fiber dynamics as part of cross-streamline migration have not yet been systematically quantified by experiments. In this article, we focus on demonstrating the effect of fiber flexibility on the migration in a confined geometry.

In this experimental study, we report the shear-induced migration of flexible fibers between two parallel plates. The fibers are non-Brownian and are confined between two transparent plates in a rheometer. Initially, the fibers are straight and are near the bottom plate due to sedimentation. The two plates counter-rotate and create a Couette flow (we note that the descriptions *shear flows* and *Couette flows* are identical in this article). Under the shear, we observe that the fibers migrate towards the center horizontal plane between the plates.

In this article, we focus on experimentally quantifying the statistical behaviors of the flexible fibers by reporting the behaviors (orientations, shapes, and dynamics) and the corresponding migration across streamlines. In Sec. 2, we describe the fiber fabrication in a microfluidic channel (Sec. 2.1) and the rheo-microscopy setup for imaging the fibers (Sec. 2.2). In Sec. 3.1, by tracking the velocities of the fibers, we demonstrate the migration of the fibers towards the horizontal center plane; bending fibers migrate faster than rolling and tumbling fibers. In Sec. 3.2, we show the orientations and shapes of the fibers in Couette flows with different magnitudes of shear rates. A dimensionless parameter Λ_{eff} [Eq. (1)] is used to characterize the effective flexibility of the fibers. Larger values of Λ_{eff} indicate larger viscous stresses and softer and smaller diameter fibers. As a result, for sufficiently small Λ_{eff}, the fibers are straight and effectively stiff. The fibers mostly tumble and roll in the flow and tend to align perpendicular to the flow direction. For an intermediate range of Λ_{eff}, the fibers start to bend and tend to align in the flow direction. At sufficiently large Λ_{eff}, the fibers bend continuously and have coil-like shapes. Finally, in Sec. 3.3, we report the time scale of the migration as a function of the effective fiber flexibility Λ_{eff}. A larger Λ_{eff} indicates more frequent bending, larger deformations, and more coiled shapes, and therefore leads to a faster migration towards the center plane between the two walls.

2 Experimental Methods

2.1 Fabrication of fibers in a microfluidic channel

We used a standard microfluidic method to fabricate the fibers, similar to previous studies[8,48–53]. The properties of the fibers, such as the length L, diameter D, and Young's modulus E, are highly controllable and reproducible. We created a uniform cylindrical jet of oligomer by flow focusing in a microfluidic channel. Ultraviolet (UV) light was shined periodically on the jet and triggered the gelation of the oligomer. We then collected the cross-linked fibers downstream at the end of the channel.

A sketch of the microfluidic device for the fiber fabrication is shown in Fig 1(a). We fabricated the device using standard soft lithography[54]. A channel made of polydimethylsiloxane (PDMS, Dow Sylgard 184; Ellsworth Adhesives) was plasma-bonded to a PDMS-coated glass slide using a Corona Surface Treater (Electro-Technic Products). The main channel was 200 μm in width and 135 μm in height. Oil solution [yellow in Fig. 1(a)] and oligomer solution [blue in Fig. 1(a)] were pumped into the the main channel from the respective inlets. As a consequence, a uniform cylindrical jet of the oligomer was focused in the main channel. The size of the jet was much smaller than the height and width of the main channel, and the jet was cylindrical due to the effect of surface tension[8]. The oil solution was, by weight, 11% Span 80 (Sigma-Aldrich) in light mineral oil (Sigma-Aldrich). The oligomer solution was, by volume, 54% poly(ethylene glycol) diacrylate (PEG-DA, molecular weight M = 575 g/mol; Sigma-Aldrich), 38% de-ionized water, and 8% 2-hydroxy-2-methylpropiophenone (photoinitiator; Sigma-Aldrich). The volumetric flow rates of the oil solution and the oligomer solution, Q_{oil} and Q_{oligomer} respectively, were controlled by syringe pumps (Harvard Apparatus). The values of Q_{oil} and Q_{oligomer} controlled the diameter of the cylindrical jet in the main channel (and therefore the diameter of the fibers). We aimed to fabricate fibers with two different diameters for comparison in the experiments. In particular, we set Q_{oil} = 0.6 ml/h and Q_{oligomer} = 0.1 (for larger diameter fibers) or 0.025 (for smaller diameter fibers) ml/h.

The surfactant (Span 80) in the oil solution stabilized the jet of the oligomer solution, which remained uniformly cylindrical for several millimeters downstream in the main channel. A UV LED (wavelength $\lambda \approx 365$ nm, input current I = 1.3 A; Thorlabs) illuminated the cylindrical jet locally and triggered the gelation in the oligomer solution. The light spot on the oligomer jet was approximately circular with a diameter $D_{\text{UV}} \approx 2.3$ mm, and the corresponding light intensity was approximately 0.03 E/(m^{2}s), which was measured in Ref. 52. The LED was turned periodically on for 20 ms and then off for 180 ms. Fibers were generated during the triggered gelation and were then collected at the end of the mi-

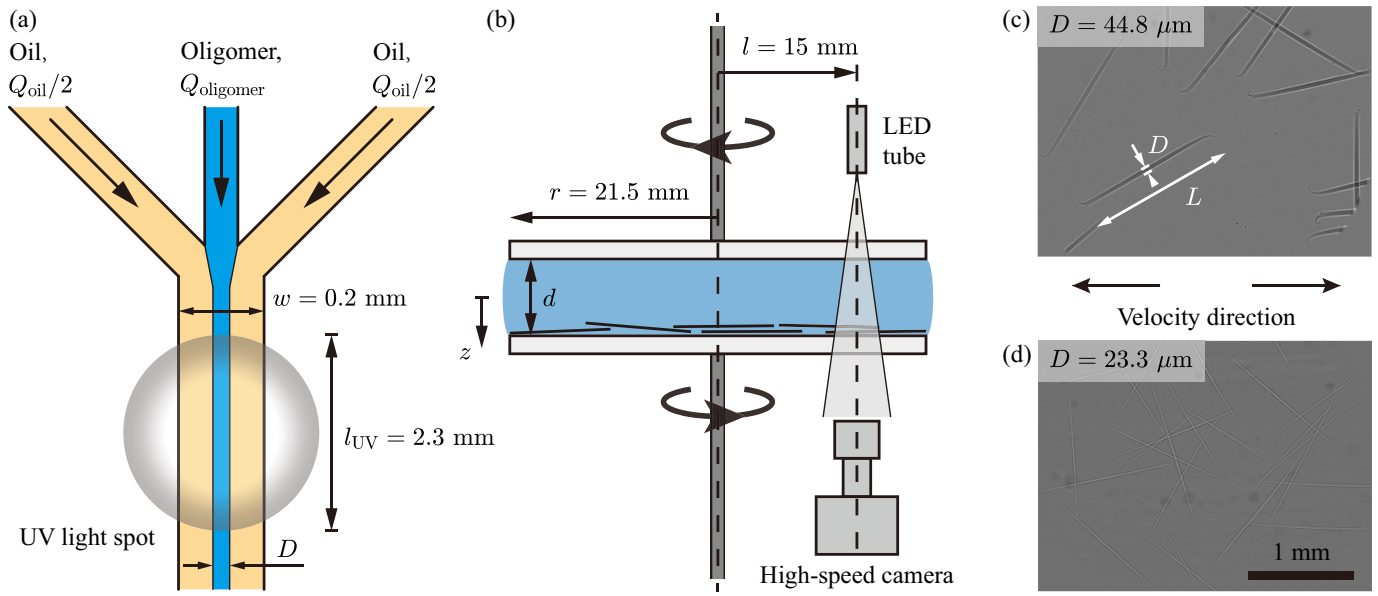

Fig. 1 Schematics of the experiments. (a) A sketch of the microfluidic setup for the fabrication of the fibers. Solutions of oil and oligomer entered the microfluidic channel and formed a cylindrical jet of the oligomer. UV light shined on the cylindrical jet and triggered the gelation of the oligomer, which resulted in cylindrical fibers that were collected downstream at the end of the channel. (b) A sketch of the rheo-microscopy setup for imaging the dynamics of the fibers in Couette flows. A suspension of the fibers was deposited between two parallel transparent plates. Initially, the fibers were near the bottom due to sedimentation. The two plates counter-rotated and created a Couette flow in the fiber suspension. The fibers were illuminated by a white LED and were imaged by a high-speed camera whose field of view was 15 mm to the center of the rheometer. (c) Image of a suspension of fibers with diameter $D = 44.8$ μm. (d) Image of a suspension of fibers with diameter $D = 23.3$ μm.

crofluidic channel. For cleaning, the fibers were washed five times in 1 wt% Tween 80 aqueous solution (Sigma-Aldrich) and twice in 0.1 wt% Tween 80 aqueous solution, and then were diluted and suspended in PEG-DA for further experiments. More quantification of the control parameters in this fabrication process can be found in Ref. 52.

As a result, we achieved two sets of fiber suspensions: (1) Suspensions of large diameter fibers with diameters $D = 44.8 \pm 0.4$ μm and length $L = 1.61 \pm 0.02$ mm. The corresponding aspect ratio $L/D \approx 36$. The volume fraction of the fibers in the suspension $\phi \approx 0.5$ vol%. (2) Suspensions of small diameter fibers with diameter $D = 23.3 \pm 2.0$ μm and length $L = 1.61 \pm 0.05$ mm. The corresponding aspect ratio $L/D \approx 69$ with volume fraction $\phi \approx 0.2$ vol%. All of the fibers were straight at rest; see Figs. 1(c,d). Note that the fibers were formed in flow and the exposure time of the UV light was shorter at the two ends of the fibers. As a consequence, near the tips, the fibers were softer, and the shapes were usually conical rather than uniformly cylindrical. The lengths of these conical regions were small compared to the total length of the fiber. Therefore, we estimated that the effect of the conical tips on the overall fiber dynamics was negligible.

One of the advantages of this fabrication method was that the produced fibers were relatively soft. The Young's modulus of the fibers $E \approx 10^5$ Pa[8,53]. As for the concentrations, both of the fiber suspensions were semi-dilute, i.e., $nDL^2 \approx 0.2 < 1$, and $nL^3 \approx 8$ (large diameter fibers) or 12 (small diameter fibers) > 1, where $n = 4\phi/(\pi D^2 L)$ is the number density of the fibers in the suspension[20]. Therefore, the interactions among the fibers and the corresponding rheological effects on the viscosities of the suspensions were insignificant, and were not the focus of this study. The viscosity of the liquid (without fibers) $\eta = 55 \pm 3$ mPas (there was a slight amount of water in the liquid). We note that there were a few larger diameter fibers observed in the suspensions of the small diameter fibers, which was due to the possible clogging in the microfluidic channel during the fabrication. These larger diameter fibers did not significantly affect the observations in the experiments, and their behaviors were not included in the measurements and processing.

2.2 Imaging the dynamics of flexible fibers in a rheo-microscope

To visualize the fiber dynamics in a Couette flow, a fiber suspension was placed in a rheo-microscopy setup; see Fig. 1(b) for a sketch. The geometry of the rheometer (MCR 702; Anton Paar) had two parallel transparent glass plates, which counter-rotated and created a Couette flow between the plates. The parallel plates were horizontal, with radius $r = 21.5$ mm. The counter-rotating speeds at the top and the bottom plates were the same (and the directions were opposite) in each experiment. To image, a white LED light guide was positioned above the fiber suspension. The light from the LED passed through a pinhole (to enhance the contrast), illuminated the fibers, and was then captured by a high-speed camera (v7.3; Phantom). A set of optical parts, such as a mirror, an objective (5×; Mitutoyo), and an extension tube, were mounted on the camera, but are not included in the sketch in Fig. 1(b). The field of view of the captured images was 3.43×2.57 mm (800×600 pixels, length × width), and the distance between the center of the field of view and the center of

the geometry $l = 15$ mm; see Fig. 1(b). Note that the refractive index of the fibers was very close to the ambient liquid. To enhance the contrast of the imaging, we set the focal plane of the camera horizontal (parallel to the plates) and slightly out-of-focus to the fibers, i.e., either above or below the fiber suspensions. This out-of-focus setting enhanced the contrast of the fibers but did not cause significant errors in the measurements of the fiber velocities; see more demonstrations and discussion in Fig. S1 in the ESI. The depth of field of the imaging was larger than the gap size d. Therefore, all of the fibers between the parallel plates in the field of view were captured.

Typical images of the large and small diameter fibers are shown, respectively, in Figs. 1(c,d). The images are the two-dimensional projections (in the horizontal plane) of the actual three-dimensional shapes of the fibers. We note that most of the fiber shapes could be imaged in the horizontal plane due to the confinement by the two walls. Initially, the fibers were straight in elastic equilibrium and oriented randomly. We aligned the setup for imaging so that the length (horizontal direction) in the field of view was in the velocity direction of the shear flow. Correspondingly, the width of the field of view was in the direction towards the center of the geometry. Gravity is orthogonal to the plane of the field of view as well as the two parallel plates. The direction of gravity is denoted as the *vertical direction* in this article. When the experiments started, the parallel plates counter-rotated and within several milliseconds accelerated to the desired speed. In the field of view, the bottom plate moved from the left to the right and the top plate moved from the right to the left.

In most of the experiments presented in this work, the gap size between the parallel plates $d = 0.5$ mm (except two experiments with $d = 1.5$ mm for comparison). Note that $d/L \approx 0.3 < 1$. The fibers were confined between the two parallel walls, which is one of the main features of this work. The effective Reynolds number in the rheometer may be estimated as[55]

$$\mathrm{Re}_{\mathrm{eff}} = \frac{\rho \dot{\gamma}_{\max} d^3}{2\eta r}, \tag{2}$$

where $\dot{\gamma}_{\max}$ was the shear rate at the edge of the parallel plate (where the shear rate was the maximum). Substituting the characteristic parameters in the experiments (Table S1 in the ESI), $\rho = 1.12 \times 10^3$ kg/m^3, $\dot{\gamma}_{\max} = 150$ s^{-1}, $d = 0.5$ mm, $\eta = 55$ mPa s, and $r = 21.5$ mm, the effective Reynolds number $\mathrm{Re}_{\mathrm{eff}} \approx 0.01 \ll 1$. Therefore, inertial effects in the experiments were negligible.

The density of the fibers was very close to but slightly larger than that of the ambient liquid. The density difference $\Delta\rho/\rho < 0.01$ and consequently sedimentation of the fibers occurred on a time scale of tens of minutes. Specifically, for the gap size $d = 0.5$ mm, it took the large diameter fibers approximately 15 minutes and the small diameter fibers approximately 30 minutes to sediment to near the bottom plate. In the experiments, we used the sedimentation of the fibers to achieve a reproducible initial condition, where the fibers were approximately on the same horizontal plane at the bottom; see the sketch in Fig. 1(b). In particular, we waited for a long time (more than 15 minutes for the large diameter fibers and 45 minutes for the small diameter fibers; see a summary of the experimental conditions in Table S1 in the ESI) until most of the fibers sank to the bottom plate.

When the experiments started, the parallel plates applied a shear stress in the suspension and the fibers detached from the bottom plate and moved in the suspension. Usually, the effect of buoyancy was negligible in the shear flow since the migration speed of the fibers was much higher than the sedimentation speed. However, when the shear rate in the suspension was relatively low, buoyancy might affect the fiber migration. Also, with a low shear rate, some fibers might remain adhered to the plates, which produced noise in the recorded movies but could be subtracted in the image processing. Both buoyancy effects and the adhered fibers will be discussed further in Sec. 3.

In the experiments, we mainly changed the local shear rate $\dot{\gamma}$ (in the field of view) to tune the effective fiber flexibility Λ_{eff}. A summary of the conditions of the experiments performed is provided in Table S1 in the ESI. For most of the experiments, we recorded the dynamics of the fiber for long periods, from the dimensionless time $\dot{\gamma}t = 0$ to at least 8000, when the migration was sufficiently developed. The corresponding representative examples of the movies are labelled Movies 1–30 in the ESI. Note that we applied a standard background subtraction process to enhance the image quality, i.e., we subtracted each image from the average intensity of the image sequence and then rescaled the subtracted images. In each experiment, not all of the fiber behaviors were identical. The reasons for the different behaviors of the fibers in the same Couette flow include (1) the shapes of the fibers at rest were not identical, e.g., the length of the fibers varied slightly by 2%, (2) the initial conditions of the fibers were not identical, e.g., the fibers oriented randomly, which led to different fiber dynamics even in the same Couette flow, as suggested by Ref. 21, and (3) the fibers were not homogeneously distributed in the suspension, potentially causing some interactions between the fibers. Since a range of fiber dynamics was observed in a single experiment, rather than tracking the behavior of a single fiber, we focused on revealing the statistical behaviors of the fibers (tens or hundreds of fibers in each experiment) as a function of the effective fiber flexibility Λ_{eff}. Usually, hundreds of fiber dynamics were captured in each experiment; see the data points in Figs. S6–S20 in the ESI.

In particular, we were interested in measuring the fiber velocities, which indicated the vertical positions of the fibers in the gap, orientations, and end-to-end lengths of the fibers. In the shear flow, fibers entered and exited the field of view and the velocities of the fibers were mainly in the flow direction. For each fiber, we recorded the period of time (i.e., the transit time) that the center of the shape of the fiber stayed in the field of view and correspondingly calculated the mean velocity of the fiber by dividing the length of the field of view (we took the distance equal to zero if the fiber entered and exited from the same side) by the recorded transit time. On the other hand, we measured the orientations and end-to-end lengths of the fibers at (close to) the centerline (perpendicular to the flow direction) of the field of view, where the dynamics of the fibers were not changing significantly. Further demonstrations and discussion of the measurements of the orientations and end-to-end lengths are provided in Fig. S2 in the ESI. The results of the measurements are displayed and

discussed in Sec. 3 and the ESI.

In each experiment, the angular rotation speed of the parallel plates was constant. As a consequence, there was a gradient of shear rate in the radial direction of the plate, i.e., the shear rate increased linearly with the distance from the center of the geometry. In particular, along the width of the field of view, i.e., perpendicular to the flow direction, the shear rate and the corresponding velocities of the shear flow varied approximately by 17% (of the mean value at the center of the field of view). To further reduce the effect of the variation of the shear rate in the experimental processing, we restricted the width of the field of view where we measured the fibers. In particular, usually, we only counted and measured the fibers that entered the field of view from the middle (e.g., the middle region with a width of 200 pixels); see a summary of the restricted widths for the experimental processing in Table S1 in the ESI. As for the radial gradient of the flow velocities, we used the local flow velocities to normalize the fiber velocities in the processing. Therefore, the radial variation of the flow velocities did not affect the quantification of the fiber velocities. However, we note that the radial gradient of the shear rate and the circular streamlines might cause a radial migration of the fibers. Still, this migration was generally not observed in the experiments, except when the gap size was large, the shear rate was high, and the time was long.

3 Experimental Results and Discussions

3.1 The migration of flexible fibers towards the center plane between the two parallel plates

In this section we focus on demonstrating the shear-induced migration of the fibers towards the horizontal center plane. We use the suspension of the large diameter fibers as an example, as shown in Figs. 2(a,b). The local shear rate in the (center of the) field of view $\dot{\gamma} = 105\ \mathrm{s}^{-1}$. The corresponding movies for the experiments are Movies 7 and 8 in the ESI.

Initially, the fibers are near the bottom plate and oriented randomly. At $t = 0$, a constant Couette flow is applied in the fiber suspension. The two parallel plates counter-rotate and create a uniform shear in the vertical direction; see the sketch in Fig. 2(c). The magnitude of the flow velocity decreases near the middle between the two plates. Fibers move and follow the shear flow. The mean velocity of a fiber, i.e., the velocity of the center of mass, indicates the vertical position of the center of the fiber in the suspension. Assuming that the mean velocity of the fiber is identical to the flow velocity (in the uniform Couette flow) at the center of the fiber, we can estimate the fiber position z according to $z/d = u/u_0$, where z is the vertical position of the center of the fiber, u is the measured velocity of the fiber, and $u_0 = \dot{\gamma}d$ is twice the speed of the moving plate (the speed of the plate is $u_0/2$). Then, $z/d = 1/2$ indicates that the fiber is at the bottom plate (where $u = u_0/2$), and $z/d = 0$ indicates that the fiber is at the center stagnation plane between the two plates. When the center of the fiber is higher than the stagnation plane, the fiber moves from the right in the field of view to the left; when the center of the fiber is lower than the stagnation plane, the fiber moves from the left to the right. The magnitude of the fiber velocity $|u|$ decreases when the fiber is closer to the middle plane.

The motions of the fibers at an early dimensionless time ($\dot{\gamma}t = 62.8$) are indicated in Fig. 2(a); the dimensionless time is also the total shear strain in the suspension. At an early time, the fibers are close to the bottom plate and all the fibers move at nearly the speed of the plate from the left in the field of view to the right. The orientations of the fibers are also random.

However, at a late time ($\dot{\gamma}t = 8715$), the behaviors of the fibers are very different; see Fig. 2(b). The magnitudes of the velocities of the fibers significantly decrease, which indicates that most of the fibers are near the stagnation plane at the middle between the parallel plates. Some fibers move from the right in the field of view to the left, which indicates that these fibers are above the stagnation plane. As for the orientations, most fibers near the stagnation plane align in the flow direction. These fibers bend and relax in the shear flow; see Movies 7 and 8 in the ESI. In contrast, some fibers do not align in the flow direction and are usually closer to the bottom plate (the speeds are higher). These fibers roll and tumble without bending. The observations of the fibers in Figs. 2(a,b) show that the fibers migrate from the bottom to the center, and suggest that the bending fibers migrate faster than the rolling and tumbling fibers.

The migration of the fibers towards the center is observed and further quantified in statistical measurements. Figure 2(d) displays the normalized velocities of the fibers u/u_0 as a function of the normalized time $\dot{\gamma}t$. The distribution of the normalized velocities implies the distribution of the vertical positions z/d of the fibers between the parallel plates. As a result, initially, the fibers are near the bottom plate, where $u/u_0 = 1/2$. In the shear flow, the fibers drift normal to the plate and migrate towards the center plane, and the mean of the distribution u/u_0 decreases with normalized time $\dot{\gamma}t$. At late times ($\dot{\gamma}t \gtrsim 3000$), the mean of the distribution approaches the center plane where $u/u_0 = 0$. In particular, most of the fibers are close to the center plane ($|u|/u_0 \lesssim 0.2$), i.e., the distribution of the fibers is not uniform in the vertical direction and more fibers are near the center. Some fibers have negative velocities ($u/u_0 < 0$), thus these fibers are above the stagnation plane, which indicates that the fibers can move across the center plane during the migration.

We note that several [two in Fig. 2(d)] fibers remain attached to the bottom plate throughout the experiments. These fibers move at the same speed as the bottom plate ($u/u_0 = 1/2$) and appear periodically in the field of view while their shapes and orientations remain unchanged. These adhered fibers are not the focus of our experiments and are thus excluded from the processing. In particular, in statistical processing (e.g., taking the average of the fiber velocities) throughout this work, we neglect the information of the fibers that are very close to the plates ($|u|/u_0 > 0.45$) after early times ($\dot{\gamma}t > 500$). This treatment provides a robust cut-off for the adhered fibers and does not miscount the detached fibers. However, we note that all of the detached and the adhered fibers are close to the bottom plate at early times, and thus, it is challenging to distinguish and reject the adhered fibers at such times. Therefore, the information of the adhered fibers might still be included in the early-time statistics, which leads to a minor error. Note that the adhered fibers are only observed in the experiments

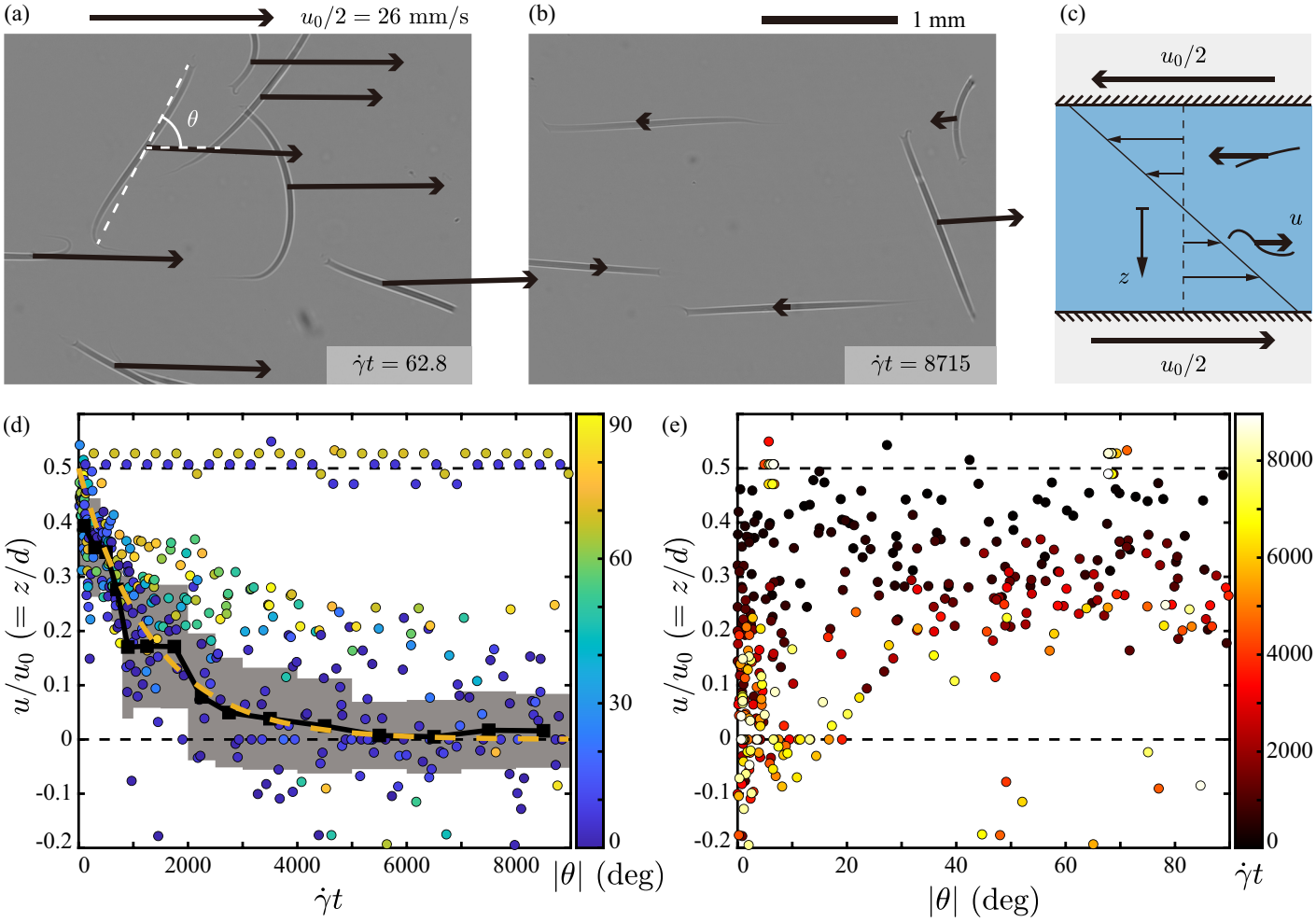

Fig. 2 Migration of fibers in a Couette flow with shear rate $\dot{\gamma} = 105$ s^{-1}, fiber diameter $D = 44.8$ μm, and the corresponding effective fiber flexibility $\Lambda_{\text{eff}} = 2 \times 10^3$. (a) The motions of the fibers at an early time, $\dot{\gamma}t = 62.8$. The arrows represent the velocities of the fibers. (b) The motions of the fibers at a late time, $\dot{\gamma}t = 8715$. (c) A schematic of the fiber motions in a Couette flow. (d) The normalized velocity of the fibers u/u_0 as a function of the normalized time (shear strain) $\dot{\gamma}t$, where $u_0 = \dot{\gamma}d$ is twice the speed of the moving plate. The circular data points show the measured velocities of the fibers. The color bar shows the corresponding alignment angles of the fibers in the shear flow $|\theta|$. The solid black line and black squares show the average velocity of the fibers, while the gray shaded area is the standard deviation of the velocity distribution. The dashed orange line shows the fitting curve of the velocity measurements using the equation $u/u_0 = \frac{1}{2}e^{-\dot{\gamma}t/\tau_0}$, where τ_0 is a fitting parameter that represents a normalized time scale for the migration. (e) The distribution of the normalized velocities of the fibers u/u_0 as a function of the alignment angles of the fibers in the shear flow $|\theta|$. The color bar shows the normalized time (shear strain) in the shear flow.

with relatively low shear rate, while all the fibers detach under a high shear.

We extract statistical results, e.g., the average of the fiber velocities, to further analyze the migration and the behaviors, e.g., the orientations, of the fibers. Fibers with higher speeds $|u|$ stay in the field of view only for shorter periods and are also observed more frequently since these fibers quickly move around in the rheometer; in contrast, fibers with lower speeds $|u|$ stay in the field of view for much longer times. Therefore, to statistically represent the behaviors of the fibers in the field of view, the properties of the fibers are weighted by the transit time that the fibers are observed. The weight function w_i is the transit time that fiber i stays in the field of view. Further, we calculate the mean value of a certain property x (e.g., x can denote the normalized velocities of the fibers, u/u_0) by $\bar{x} = \sum_i x_i w_i'$, where $\bar{x}$ is the mean value of the property, x_i is the value of the property of fiber i, and $w_i' = w_i / \sum_i w_i$ is the normalized weight function for fiber i. The corresponding standard deviation is $\left(\sum_i w_i' \sigma_i^2\right)^{1/2}$, and the standard error is $\left(\sum_i w_i'^2 \sigma_i^2\right)^{1/2}$, where $\sigma_i = x_i - \bar{x}$ is the deviation (from the mean value) of fiber i.

To analyze the migration of the fibers, we calculate the mean values of the normalized velocities of the fibers $< u/u_0 >$ as a function of the dimensionless time $\dot{\gamma}t$; see the solid black line and black squares in Fig. 2(d). Note that each mean value [black squares in Fig. 2(d)] represents the average value of the fiber velocities in a sub-region of $\dot{\gamma}t$ in the experiments, e.g., $0 \le \dot{\gamma}t < 200$ for the first square. As a result, the mean value of the normalized velocities typically decreases in time and approaches zero at late times, which confirms the migration of the fibers towards the stagnation plane in the shear flow. The migration is faster at early times when fibers are near the bottom plate and is slower at late

times when the fibers are near the center plane.

To further characterize the migration, we fit the migration results according to $u/u_0 = \frac{1}{2}e^{-\dot{\gamma}t/\tau_0}$, where τ_0 represents the normalized time scale for the migration. In the fitting, the velocity of each fiber is weighted by w_i, which is the transit time that the fiber is in the field of view. In particular, $\tau_0 \approx 1.3 \times 10^3$ for the experiment presented in this section, and the exponential decay equation agrees well with the trend of migration in the experimental measurements; see the dashed orange line in Fig. 2(d). We will discuss the normalized time scale for the migration τ_0 as a function of the effective fiber flexibility Λ_{eff} in Sec. 3.3.

The migration of the fibers is associated with the detailed dynamics, e.g., the orientation of the fibers. For example, at late times [$\dot{\gamma}t \gtrsim 3000$, in Fig. 2(d)], the fibers at the horizontal center plane ($u/u_0 \lesssim 0.1$) are mostly aligned in the velocity direction [blue circles in Fig. 2(d)]. In contrast, the fibers that are not aligned in the velocity direction still migrate towards the center plane but are closer to the bottom plate. Note that the color bar in Fig. 2(d) represents the alignment angle of the fibers in the flow direction $|\theta|$. $|\theta| = 0$ indicates that the fiber is aligned in the flow direction (the horizontal direction in the field of view), and $|\theta| = 90$ degrees indicates that the fiber is perpendicular to the shear flow. There is no significant difference between a negative value and a positive value of θ since the geometry is mainly symmetric.

The distribution of the orientations of the fibers is shown in Fig. 2(e), where the color bar indicates the normalized time $\dot{\gamma}t$. Initially [black circles in Fig. 2(e)], the fibers are near the bottom plate ($u/u_0 = 1/2$) and oriented randomly (black circles distribute approximately uniformly from $|\theta| = 0$ to 90 degrees). At late times [bright circles in Fig. 2(e)], most of the fibers are near the left bottom corner (where $u/u_0 = 0$ and $|\theta| = 0$), which indicates that the fibers mostly migrate toward the center and align in the flow direction. Several fibers are not aligned in the flow direction and are closer to the bottom plate. We note that for the results presented in this section, most of the fibers tend to align in the flow direction (more precisely, the alignment of the fiber is dependent on its initial condition and the effective fiber flexibility, which is suggested in Ref. 21 and will be discussed further in Sec. 3.2).

Our imaging of the fibers is a two-dimensional projection in the horizontal plane of the three-dimensional fiber shapes. According to our observations (e.g., Movies 7 and 8 in the ESI), the fibers tend to bend when aligned in the flow direction. In contrast, the fibers tend to roll and tumble when they are perpendicular to the flow direction. The bending fibers exhibit more out-of-plane motion (in the vertical direction, orthogonal to the plane of the field of view), i.e., the length (projection) of the fiber in the orthogonal direction changes significantly when bending[21]. Further, our observation shows that the mean velocities of the fibers remain constant when the fibers do not bend; in contrast, when the fibers bend, the mean velocity rapidly changes in time, indicating that the vertical positions of the fibers z change during the bending. The bending deformations normal to the walls induce hydrodynamic interaction between the walls and the fibers, which breaks the symmetry of the system and leads to the irreversibility of the flow[15,44]. On the other hand, potentially, a bending fiber might make direct contact with the wall and bounce away from the wall, which is the so-called *pole-vault* motion[33,35,38,42,43]. As a consequence of the hydrodynamic interaction and the possible direct contact with the wall, bending fibers drift away from the walls, similar to the drifting of deformable droplets away from the walls in shear flows[34,36,37]. A demonstration of the tracking of a single bending fiber is in Fig. S3 and Movie 31 in the ESI. To summarize the observations, more frequent and larger bending deformations lead to faster migration away from the walls.

The strength of the shear flow determines the behaviors of the fibers and thus influences the migration of the fibers. In Sec. 3.2, we will further discuss the orientations and shapes of the fibers with different effective fiber flexibilities Λ_{eff}. The corresponding migration of the fibers with different Λ_{eff} will be discussed in Sec. 3.3.

3.2 The orientations and shapes of the fibers

In this section, we focus on demonstrating the orientations and shapes of the fibers under different shear stresses. To expand the parameter space, we use both large diameter fibers ($D = 44.8$ μm) and small diameter fibers ($D = 23.3$ μm), and tune the shear rate $\dot{\gamma} \approx 1$ to 2×10^3 s^{-1}. The corresponding effective fiber flexibilities $\Lambda_{\text{eff}} \approx 2 \times 10^1$ to 5×10^5 [by Eq. (1)]; see a summary of the experiments and the corresponding conditions in Table S1 in the ESI.

Snapshots of the fibers in Couette flows with different effective fiber flexibilities Λ_{eff} are shown in Figs. 3(a-f), where all of the snapshots are taken at the normalized time $\dot{\gamma}t \approx 4000$. As a result, we can compare the behaviors of the fibers with different Λ_{eff}. We identify mainly three different ranges of Λ_{eff}.

At a low effective fiber flexibility ($\Lambda_{\text{eff}} \lesssim 2 \times 10^2$), the shear rate $\dot{\gamma}$ is low, and the fibers behave like rigid objects in flow; see Fig. 3(a) and the corresponding movies labelled Movies 1 and 2 in the ESI. Many fibers are adhered to the plates since the adhesion to the wall is comparable to the shear stress. The detached fibers mostly roll and tumble following Jeffrey-like orbits[56]. The fibers are mainly perpendicular to the shear flow, and the migration is slow (on the scale of the dimensionless time, $\dot{\gamma}t$).

For an intermediate range of the effective flexibility ($2 \times 10^2 \lesssim \Lambda_{\text{eff}} \lesssim 2 \times 10^4$), the fibers exhibit some deformations and tend to align in the flow direction; see Figs. 3(b-d) and the corresponding Movies 5, 6, 11, 12, 17, and 18 in the ESI. The fibers bend and then relax in the shear flow but remain straight most of the time. Still, a small portion of the fibers are perpendicular to the flow, where they roll and tumble in the shear flow. Overall, the migration speed is moderate, and the mean positions of the fibers are close to the horizontal center plane at late times ($\dot{\gamma}t \approx 4000$).

In the large effective flexibility range ($\Lambda_{\text{eff}} \gtrsim 2 \times 10^4$), the fibers exhibit significant deformations; see Figs. 3(e,f) and the corresponding Movies 21, 22, 25, and 26 in the ESI. The fibers bend continuously and seldom relax to straight, which leads to a coiled shape. The orientations and end-to-end vector of the fibers are random due to the coiled shape. The migration of the fibers is fast and the fibers are typically near the center plane within $\dot{\gamma}t \approx 1000$. Moreover, all the fibers are closer to the middle plane due to the

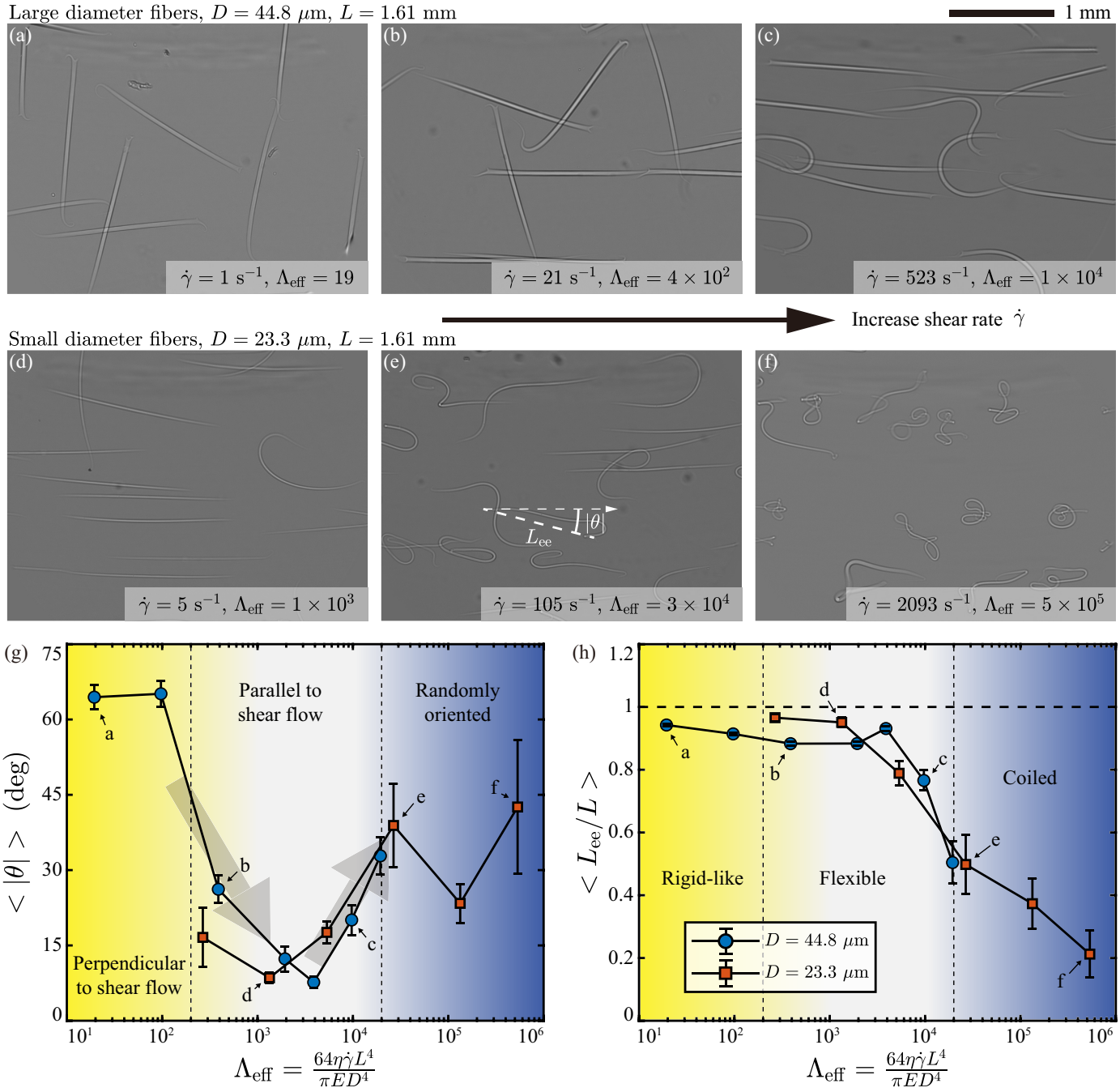

Fig. 3 The structure of the fibers at late times. The images are, respectively, large diameter fibers ($D = 44.8$ μm) in Couette flows with the shear rates $\dot{\gamma}$ = (a) 1, (b) 21, and (c) 523 s^{-1}, and small diameter fibers ($D = 23.3$ μm) with the shear rates $\dot{\gamma}$ = (d) 5, (e) 105, and (f) 2093 s^{-1}. The snapshots are taken at the normalized time $\dot{\gamma}t \approx 4000$; in order to achieve snapshots with a clean background and enough fibers in each field of view, the exact normalized time of the snapshots are, respectively, $\dot{\gamma}t$ = (a) 4156, (b) 4084, (c) 3889, (d) 3982, (e) 3925, and (f) 3901. (g) The mean value of the alignment angle of the fibers $< |\theta| >$ as a function of the effective fiber flexibility $\Lambda_{\rm eff}$. (h) The mean value of the normalized end-to-end length of the fibers $< L_{ee}/L >$ as a function of the effective fiber flexibility $\Lambda_{\rm eff}$. The error bars in (g) and (h) represent the standard errors.

continuous bending of the fibers and the resulting drift away from the walls; e.g., see the distributions of the normalized velocities of the fibers u/u_0 in Figs. S16 and S17 in the ESI.

Further, we process the statistical values of the fibers to characterize the behaviors of the fibers in shear flows. In particular, we are interested in the mean values of the alignment angle $< |\theta| >$ and the normalized end-to-end length $< L_{ee}/L >$, which are, respectively, the signatures of the orientations and shapes of the fibers. For comparison, we calculate the mean values of the measurements from the normalized time $\dot{\gamma}t = 2000$ to 4000 in each experiment. The statistical results are displayed in Figs. 3(g,h), as a function of the effective fiber flexibility $\Lambda_{\rm eff}$. The results for the large and small diameter fibers are similar.

In the low effective flexibility range ($\Lambda_{\rm eff} \lesssim 2 \times 10^2$), the mean

value of the alignment angle is large, $<|\theta|> \approx 60$ degrees, which indicates that the fibers are mainly perpendicular to the shear flow. In the intermediate effective flexibility range ($2\times10^2 \lesssim \Lambda_{\text{eff}} \lesssim 2\times10^4$), $<|\theta|>$ sharply decreases with Λ_{eff} until it reaches a minimum at $\Lambda_{\text{eff}} \approx 4\times10^3$. At the minimum, $<|\theta|> \approx 10$ degrees and the fibers are mostly aligned in the flow direction. When Λ_{eff} further increases, fibers bend more frequently and transition from straight to coiled shapes. $<|\theta|>$ increases with Λ_{eff} until $<|\theta|> \approx 45$ degrees (the orientation is fully random) in the large effective flexibility range ($\Lambda_{\text{eff}} \gtrsim 2\times10^4$). We note that after the shear flow with large Λ_{eff} ceases, the fibers relax to their straight shapes and orient randomly. Applying a high shear in the fiber suspension is a reproducible protocol to achieve homogeneous fiber suspensions (with respect to the fiber orientations).

As for the normalized end-to-end length of the fibers $<L_{\text{ee}}/L>$, the fibers are slightly curved ($<L_{\text{ee}}/L> \approx 1$) in the low and intermediate effective flexibility ranges. When Λ_{eff} increases, the fibers bend more frequently, and the shapes of the fibers are coiled. As a result, $<L_{\text{ee}}/L>$ decreases with Λ_{eff}. Further, $<L_{\text{ee}}/L> \approx 0.2$ at $\Lambda_{\text{eff}} \approx 5\times10^5$, which indicates that the fibers are coiled and compact under high shear stresses.

The statistical results of $<|\theta|>$ and $<L_{\text{ee}}/L>$ characterize the behaviors of the fibers with different flexibilities. We note that both $<|\theta|>$ and $<L_{\text{ee}}/L>$ represent the mean values (therefore, the averaged behaviors) of the fibers, and the distributions of the values may be very broad. A comparison of the distributions of $|\theta|$ and $<L_{\text{ee}}/L>$ as a function of Λ_{eff} is provided in Fig. S4 in the ESI. The comparison shows distinct differences in the distributions with different effective flexibilities.

3.3 The time scale for the migration of the flexible fibers

In this section, we focus on demonstrating the migration of the flexible fibers with different effective fiber flexibilities. The detailed conditions for the experiments are provided in Table S1 in the ESI.

The migration of the large diameter fibers in Couette flows with different shear rates $\dot{\gamma}$ is shown in Fig. 4(a). The mean velocities of the fibers $<u/u_0>$ are presented as a function of the normalized time $\dot{\gamma}t$. The statistical results show that $<u/u_0>$ decreases with $\dot{\gamma}t$ and approaches zero at late times. Also, an increase in the effective fiber flexibility Λ_{eff} leads to a faster fiber migration towards the center plane. Note that the migration of the smaller diameter fibers is similar to these results; see Fig. S5 in the ESI.

As discussed in Section 3.1, we use the exponential decay equation $u/u_0 = \frac{1}{2}e^{-\dot{\gamma}t/\tau_0}$ to fit the positions of the fibers, where τ_0 represents the normalized time scale for the migration of the fibers and is a function of Λ_{eff}. The exponential decay equation describes the migration of the fibers well [the dashed colored lines are close to their respective solid colored lines in Figs. 4(a) and S5 in the ESI], except in the experiments where the shear rate is low and the effect of buoyancy matters [$\dot{\gamma} = 1$ and $5\ \text{s}^{-1}$ in Fig. 4(a)]. The fitted values of τ_0 with the shear rates $\dot{\gamma} = 1$ and $5\ \text{s}^{-1}$ (in the suspensions of large diameter fibers) are not considered in any further analysis of $\tau_0(\Lambda_{\text{eff}})$.

By fitting the exponential decay equation, we estimate the normalized time scale for fiber migration τ_0 with different effective flexibilities Λ_{eff}; see $\tau_0(\Lambda_{\text{eff}})$ in Fig. 4(b). The responses of the large and small diameter fibers are similar. τ_0 responds relatively slowly to the variation of Λ_{eff}: τ_0 decreases from approximately 2×10^3 to 4×10^2, which is a factor of 5, while Λ_{eff} increases from approximately 1×10^2 to 1×10^6, which is a factor of $O(10^4)$. A power-law fit in Fig. 4(b) shows that $\tau_0 \propto \Lambda_{\text{eff}}^{-0.19\pm0.12}$ (with 95% confidence bounds).

In Couette flows, the fibers that are more likely to bend migrate faster towards the horizontal middle plane between the two plates. The main reasons for the observed faster migration are: (1) more bendable fibers, e.g., smaller diameter fibers and higher shear stress, tend to align more in the flow direction and bend in the shear flow[21]; (2) more frequent bending, with larger deformations in the shear flow, leads to faster drifting away from the walls. Note again that the bending deformation leads to the irreversibility of the flow and the drifting of the fibers, which is similar to the drifting of deformable droplets in shear flows[34,36,37]; and (3) the radius of curvature of the fiber decreases when the shear stress increases[22]. As a consequence, the fibers that are more likely to bend are more coiled, which decrease the effective hydrodynamics ratios (effective aspect ratios) and lead to more frequent tumbling, rolling, and bending behaviors (bending, tumbling, and rolling are coupled under a high shear). Note that (1), (2), and (3), respectively, highlight the orientations, dynamics, and shapes of the fibers in the shear flows.

Further, to demonstrate the effect of confinement from the walls, we perform control experiments with the gap size d = 1.5 mm (three times the gap size that is mainly used in this study). The resulting migration of the fibers with the large gap size (d = 1.5 mm) is very similar to those with the gap size d = 0.5 mm. For example, the corresponding normalized time scales τ_0 for d = 0.5 and 1.5 mm are almost identical; see the blue circles, the yellow upward-pointing triangle, and the purple downward-pointing triangle in Fig. 4(b). Also, we add 10 vol% water in the fiber suspension to enhance the buoyancy, and no significant difference in the fiber migration is observed. More comparisons of the velocity distributions are in Fig. S20 in the ESI.

As a result, in the limit that the fibers are confined between the parallel plates ($D \ll d$ and $L \approx d$), the gap size does not significantly affect the dimensionless time scale for the migration. We highlight that in our experiments, the fibers are affected by the existence of both plates (i.e., the top plate as well as the bottom plate). The bending of the fibers leads to hydrodynamic interactions between both plates, but the drift away from the closer plate is usually stronger, which leads to the migration towards the center. Therefore, in this confined geometry, the migration of the fibers is not significantly affected by the gap size. The gap size d is expected to strongly influence the fiber migration in the limit that $d \gg L$. The threshold and the transition of the confinement of the geometry and the corresponding fiber migration are very interesting prospects for further investigations.

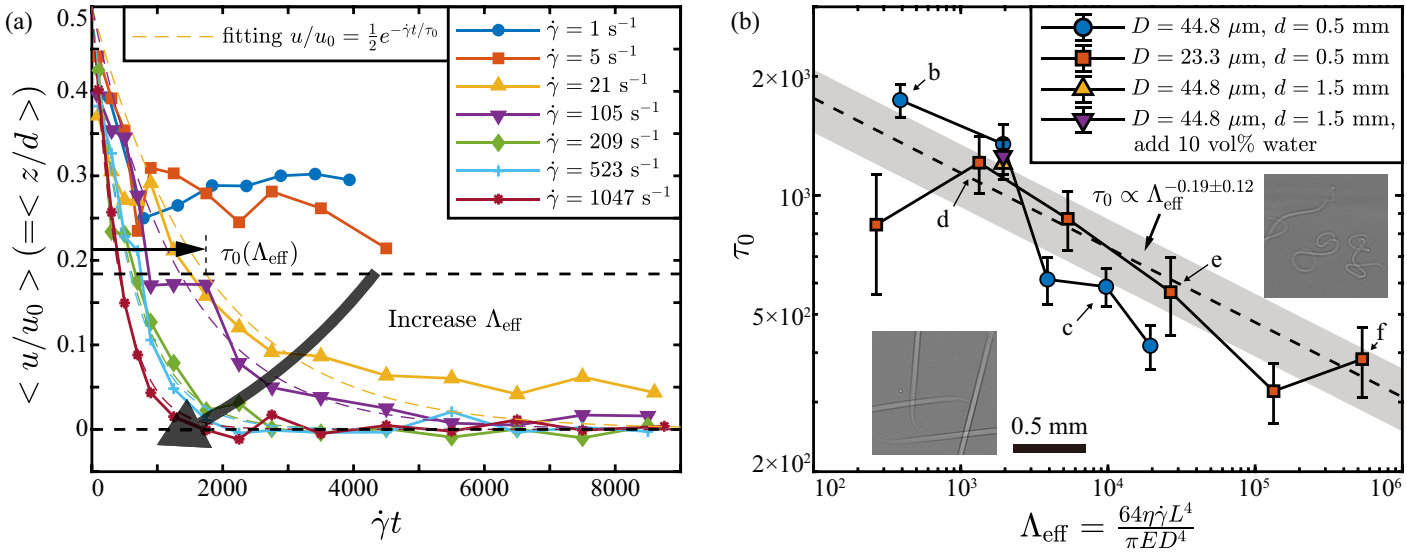

Fig. 4 The normalized time scale for the shear-induced migration of the fibers. (a) The normalized mean velocity of the large diameter fibers ($D = 44.8$ μm) $< u/u_0 >$ as a function of the normalized time (shear strain) $\dot{\gamma}t$. The shear rate of the flow $\dot{\gamma} = 1$ (circles), 5 (squares), 21 (upward-pointing triangles), 105 (down-pointing triangles), 209 (diamonds), 523 (plus signs), and 1047 (asterisks) s^{-1}, respectively. The corresponding effective flexibility $\Lambda_{\rm eff} = 2\times10^1$, 1×10^2, 4×10^2, 2×10^3, 4×10^3, 1×10^4, and 2×10^4, respectively. The dashed colored lines show the corresponding fit using the exponential decay equation $u/u_0 = \frac{1}{2}e^{-\dot{\gamma}t/\tau_0}$, where τ_0 represents the normalized time scale for the shear-induced migration of the fibers. (b) The fitted normalized time scale for the migration τ_0 as a function of the effective fiber flexibility $\Lambda_{\rm eff}$. The experimental conditions are, respectively, $D = 44.8$ μm and $d = 0.5$ mm (circles), $D = 23.3$ μm and $d = 0.5$ mm (squares), and $D = 44.8$ μm and $d = 1.5$ mm (triangles). The error bars represent the fitted τ_0 with 95% confidence bounds. The dashed line shows the power-law fitting of $\tau_0(\Lambda_{\rm eff})$, and the gray shaded region represents $\tau_0 \propto \Lambda_{\rm eff}^{-0.19}$ with 95% confidence bounds. The two snapshots are, respectively, from Figs. 3(a) and 3(f) (cropped).

4 Conclusion

In this experimental study, we reported the shear-induced migration of the suspensions of flexible fibers between two parallel plates. We produced the fiber suspensions using a standard microfluidic method, which controlled the lengths, diameters, and elasticities of the fabricated fibers. We then used a rheo-microscopy setup to image the dynamics and the migration of the fibers in Couette flows. The fibers were non-Brownian and were confined between the two plates. We focused on demonstrating the statistical behaviors of the fibers, for example, the mean values of the positions, alignment angles, and end-to-end lengths of the fibers. The dimensionless parameter $\Lambda_{\rm eff}$ [Eq. (1)], which represents the competition between the shear stress and bending modulus, was used to characterize the flexibilities of the fibers. As a result, in the shear flow, the fibers, which were initially at the bottom plate, migrated towards the horizontal center plane between the two counter-rotating parallel walls. The fibers that are more likely to bend migrated faster. For sufficiently small $\Lambda_{\rm eff}$, the fibers were rigid, mainly tumbled and rolled in the shear flow, and the migration speed was low. For an intermediate range of $\Lambda_{\rm eff}$, the fibers tended to align in the flow direction and bend, which led to a moderate migration speed. For sufficiently large $\Lambda_{\rm eff}$, the fibers bent continuously, exhibited coil-like shapes, and the migration speed was fast. Finally, an empirical exponential decay equation and a corresponding normalized time scale for the migration were presented, which described well the migration of the fibers under different shear stresses.

This work highlights the effect of flexibility on the shear-induced migration with the confinement from the two walls. Further, this work correlates the migration with the dynamics and the structures of the fibers. We find the following directions constructive and worth considering for further investigations:

(1) Theoretical modeling and numerical computations on the flexible fiber dynamics. We note that the conditions in the experiments are usually not ideal. For example, typically fibers are not perfectly straight at rest, not uniform at the two ends, not perfectly placed and oriented as the initial condition, or not ideally dilute and might induce complex fiber-fiber interactions. Also, in the experiments, it is challenging to reconstruct the three-dimensional shapes and dynamics of the fibers, and the imaging is usually a two-dimensional projection of the fibers in the horizontal plane. Numerical computations will help to understand the three-dimensional dynamics of the fibers. Further, it would be helpful to analyze the interaction between the fibers and the walls and estimate the magnitude of the drifting force away from the walls with different effective fiber flexibilities.

(2) Tracking the dynamics of the fibers. In this study, we focus on the statistical behaviors of the fibers. We note that tracking the dynamics of individual fibers would provide new information, for example, the frequencies of the fiber bending, the trajectories of the end-to-end vectors of the fibers, and the local curvatures along the fibers as a function of time. Tracking the fibers would be beneficial to characterize the fiber dynamics and even the fiber-fiber interactions in Couette flows with different shear rates. The observations in the experiments show that the fibers tend to bend simultaneously. Though the periods of motions of the bending fibers are similar (the fibers might bend simultaneously since they have similar frequencies), we expect that

the hydrodynamic interactions of the fibers might also be a possible mechanism, e.g., a bending fiber triggers the perturbation of another neighboring fiber, which leads to simultaneous bending, and remains as a potential topic for further investigations. Whether the bending fibers are in direct contact with the walls is another interesting question. Moreover, the comparisons of the dynamics and the migration among flexible fibers, rigid rods, and spherical particles would be constructive.

(3) The rheological properties of the fiber suspensions. In this work, we focus on the microscopic behavior of the fibers. The macroscopic rheological properties of the fiber suspensions under different shear stresses are another interesting aspect for future investigations (especially for more concentrated fiber suspensions). In the shear flow, the fibers migrate towards the center and increase the local concentration near the middle plane. Therefore, at late times, we expect that there will be more fiber-fiber interactions near the middle plane, and the fibers might even entangle with each other and create gel-like structures[8]. Characterizing a typical time scale when the fibers migrate and entangle would be of practical interests. Further correlating the macroscopic rheological properties of the fiber suspension with the microscopic dynamics of the fibers would be fundamental and even constructive for building guidelines for fiber-based soft materials.

Data Availability

An extended version of the movies, the datasets, and the Matlab codes to support this study are available at https://doi.org/10.34770/cp0y-ee27.

Author Contributions

N.X., J.K.N., and H.A.S. initiated this work. N.X. performed the experiments and processed the data. N.X., J.K.N., and H.A.S. discussed the results and wrote the paper.

Conflicts of interest

There are no conflicts to declare.

Acknowledgment

The authors thank Jiarong Hong and Antonio Perazzo for helpful discussions on imaging the fibers, and Maria Ekiel-Jeżewska, Agnieszka Słowicka, and Paweł Sznajder for fruitful discussions on the evolution of the fiber orientations in a shear flow. The authors thank the anonymous referees for their valuable suggestions and recommendations for improvement of the original manuscript. N.X. acknowledges Princeton University through a Charlotte Elizabeth Procter Fellowship. The authors acknowledge support from NSF grant CMMI-1661672. The authors acknowledge the use of Princeton's Imaging and Analysis Center, which is partially supported through the Princeton Center for Complex Materials (PCCM), a National Science Foundation (NSF)-MRSEC program (DMR-2011750).

Notes and references

1 O. Du Roure, A. Lindner, E. N. Nazockdast and M. J. Shelley, *Annu. Rev. Fluid Mech.*, 2019, **51**, 539–572.

2 G. I. Taylor, *Proc. R. Soc. Lond. A*, 1951, **209**, 447–461.

3 E. Lauga, *Phys. Rev. E*, 2007, **75**, 041916.

4 J. Alvarado, J. Comtet, E. De Langre and A. E. Hosoi, *Nat. Phys.*, 2017, **13**, 1014–1019.

5 W. Gilpin, M. S. Bull and M. Prakash, *Nat. Rev. Phys.*, 2020, **2**, 74–88.

6 T. T. Perkins, D. E. Smith and S. Chu, *Science*, 1997, **276**, 2016–2021.

7 E. Han, L. Zhu, J. W. Shaevitz and H. A. Stone, *Proc. Natl. Acad. Sci. U.S.A.*, 2021, **118**, e2022000118.

8 A. Perazzo, J. K. Nunes, S. Guido and H. A. Stone, *Proc. Natl. Acad. Sci. U.S.A.*, 2017, **114**, E8557–E8564.

9 O. L. Forgacs and S. G. Mason, *J. Colloid Sci.*, 1959, **14**, 473–491.

10 A. Salinas and J. F. T. Pittman, *Polym. Eng. Sci.*, 1981, **21**, 23–31.

11 J. A. Odell, A. Keller and Y. Rabin, *J. Chem. Phys.*, 1988, **88**, 4022–4028.

12 P. LeDuc, C. Haber, G. Bao and D. Wirtz, *Nature*, 1999, **399**, 564–566.

13 C. F. Schmid, L. H. Switzer and D. J. Klingenberg, *J. Rheol.*, 2000, **44**, 781–809.

14 L. E. Becker and M. J. Shelley, *Phys. Rev. Lett.*, 2001, **87**, 198301.

15 A. M. Słowicka, E. Wajnryb and M. L. Ekiel-Jeżewska, *Eur. Phys. J. E*, 2013, **36**, 1–12.

16 I. Kirchenbuechler, D. Guu, N. A. Kurniawan, G. H. Koenderink and M. P. Lettinga, *Nat. Commun.*, 2014, **5**, 1–8.

17 C. Brouzet, G. Verhille and P. Le Gal, *Phys. Rev. Lett.*, 2014, **112**, 074501.

18 A. Farutin, T. Piasecki, A. M. Słowicka, C. Misbah, E. Wajnryb and M. L. Ekiel-Jeżewska, *Soft Matter*, 2016, **12**, 7307–7323.

19 Y. Liu, B. Chakrabarti, D. Saintillan, A. Lindner and O. Du Roure, *Proc. Natl. Acad. Sci. U.S.A.*, 2018, **115**, 9438–9443.

20 J. E. Butler and B. Snook, *Annu. Rev. Fluid Mech.*, 2018, **50**, 299–318.

21 A. M. Słowicka, H. A. Stone and M. L. Ekiel-Jeżewska, *Phys. Rev. E*, 2020, **101**, 023104.

22 P. J. Żuk, A. M. Słowicka, M. L. Ekiel-Jeżewska and H. A. Stone, *J. Fluid Mech.*, 2021, **914**, A31.

23 S. Goto, H. Nagazono and H. Kato, *Rheol. Acta*, 1986, **25**, 119–129.

24 M. Keshtkar, M. C. Heuzey and P. J. Carreau, *J. Colloid Sci.*, 2009, **53**, 631–650.

25 V. Shankar, M. Pasquali and D. C. Morse, *J. Rheol.*, 2002, **46**, 1111–1154.

26 A.-K. Tornberg and M. J. Shelley, *J. Comput. Phys.*, 2004, **196**, 8–40.

27 R. Scirocco, J. Vermant and J. Mewis, *J. Non-Newton. Fluid Mech.*, 2004, **117**, 183–192.

28 R. Pasquino, F. Snijkers, N. Grizzuti and J. Vermant, *Rheol. Acta*, 2010, **49**, 993–1001.

29 G. D'Avino, F. Greco and P. L. Maffettone, *Annu. Rev. Fluid Mech.*, 2017, **49**, 341–360.

30 G. Segre and A. Silberberg, *Nature*, 1961, **189**, 209–210.

31 J. F. Morris, *Phys. Rev. Fluids*, 2020, **5**, 110519.

32 Z. Varga, V. Grenard, S. Pecorario, N. Taberlet, V. Dolique, S. Manneville, T. Divoux, G. H. McKinley and J. W. Swan, *Proc. Natl. Acad. Sci. U.S.A.*, 2019, **116**, 12193–12198.

33 C. A. Stover and C. Cohen, *Rheol. Acta*, 1990, **29**, 192–203.

34 J. R. Smart and D. T. Leighton Jr., *Phys. Fluids A*, 1991, **3**, 21–28.

35 K. B. Moses, S. G. Advani and A. Reinhardt, *Rheol. Acta*, 2001, **40**, 296–306.

36 M. Abkarian, C. Lartigue and A. Viallat, *Phys. Rev. Lett.*, 2002, **88**, 068103.

37 M. Abkarian and A. Viallat, *Biophys. J.*, 2005, **89**, 1055–1066.

38 N. A. Mody and M. R. King, *Phys. Fluids*, 2005, **17**, 113302.

39 R. G. Larson, *J. Rheol.*, 2005, **49**, 1–70.

40 E. S. G. Shaqfeh, *J. Non-Newton. Fluid Mech.*, 2005, **130**, 1–28.

41 D. Saintillan, E. S. G. Shaqfeh and E. Darve, *J. Fluid Mech.*, 2006, **557**, 297–306.

42 M. Zurita-Gotor, J. Bławzdziewicz and E. Wajnryb, *J. Rheol.*, 2007, **51**, 71–97.

43 J. Park and J. E. Butler, *J. Fluid Mech.*, 2009, **630**, 267–298.

44 J. W. Swan and J. F. Brady, *Phys. Fluids*, 2010, **22**, 103301.

45 M. D. Graham, *Annu. Rev. Fluid Mech.*, 2011, **43**, 273–298.

46 D. J. Pine, J. P. Gollub, J. F. Brady and A. M. Leshansky, *Nature*, 2005, **438**, 997–1000.

47 B. Rallabandi, N. Oppenheimer, M. Y. B. Zion and H. A. Stone, *Nat. Phys.*, 2018, **14**, 1211–1215.

48 Y. Jun, E. Kang, S. Chae and S. Lee, *Lab Chip*, 2014, **14**, 2145–2160.

49 J. K. Nunes, K. Sadlej, J. I. Tam and H. A. Stone, *Lab Chip*, 2012, **12**, 2301–2304.

50 J. K. Nunes, H. Constantin and H. A. Stone, *Soft Matter*, 2013, **9**, 4227–4235.

51 J. K. Nunes, C.-Y. Wu, H. Amini, K. Owsley, D. Di Carlo and H. A. Stone, *Adv. Mater.*, 2014, **26**, 3712–3717.

52 M. Slutzky, H. A. Stone and J. K. Nunes, *Soft Matter*, 2019, **15**, 9553–9564.

53 J. K. Nunes, J. Li, I. M. Griffiths, B. Rallabandi, J. Man and H. A. Stone, *Soft matter*, 2021, **17**, 3609–3618.

54 Y. Xia and G. M. Whitesides, *Annu. Rev. Mater. Sci.*, 1998, **28**, 153–184.

55 R. H. Ewoldt, M. T. Johnston and L. M. Caretta, *Complex fluids in biological systems*, Springer, 2015, pp. 207–241.

56 G. B. Jeffery, *Proc. R. Soc. Lond. A*, 1922, **102**, 161–179.